Article

Homomeric chains of intermolecular bonds scaffold octahedral germanium perovskites

Amin Morteza Najarian[1], Filip Dinic[2,3], Hao Chen[1], Randy Sabatini[1], Chao Zheng[1], Alan Lough[3], Thierry Maris[4], Makhsud I. Saidaminov[5], F. Pelayo García de Arquer[6], Oleksandr Voznyy[2,3], Sjoerd Hoogland[1] & Edward H. Sargent[1✉]

Perovskites with low ionic radii metal centres (for example, Ge perovskites) experience both geometrical constraints and a gain in electronic energy through distortion; for these reasons, synthetic attempts do not lead to octahedral $[GeI_6]$ perovskites, but rather, these crystallize into polar non-perovskite structures[1–6]. Here, inspired by the principles of supramolecular synthons[7,8], we report the assembly of an organic scaffold within perovskite structures with the goal of influencing the geometric arrangement and electronic configuration of the crystal, resulting in the suppression of the lone pair expression of Ge and templating the symmetric octahedra. We find that, to produce extended homomeric non-covalent bonding, the organic motif needs to possess self-complementary properties implemented using distinct donor and acceptor sites. Compared with the non-perovskite structure, the resulting $[GeI_6]^{4-}$ octahedra exhibit a direct bandgap with significant redshift (more than 0.5 eV, measured experimentally), 10 times lower octahedral distortion (inferred from measured single-crystal X-ray diffraction data) and 10 times higher electron and hole mobility (estimated by density functional theory). We show that the principle of this design is not limited to two-dimensional Ge perovskites; we implement it in the case of copper perovskite (also a low-radius metal centre), and we extend it to quasi-two-dimensional systems. We report photodiodes with Ge perovskites that outperform their non-octahedral and lead analogues. The construction of secondary sublattices that interlock with an inorganic framework within a crystal offers a new synthetic tool for templating hybrid lattices with controlled distortion and orbital arrangement, overcoming limitations in conventional perovskites.

Pb-based halide perovskites show desirable optoelectronic properties: long carrier diffusion lengths, high charge carrier mobilities and high absorption coefficients[9–12]. There exists intensive interest in Pb-free materials that exhibit comparable properties[3,5,13–16]. For Pb-based perovskites, the character of the valence band maximum involves the $6s$ orbital of M^{2+} (s^*) and the conduction band minimum from the $6p$ orbital (p^*)[17] (Fig. 1a); this orbital arrangement plays an important role in the impressive properties of Pb-based perovskites. In this regard, alternatives to Pb include the group IVa elements Sn and Ge[3,5]; however, when the ionic radii of the metal centre decrease from Pb ($6s^2$) to Ge ($4s^2$), two effects challenge the formation of the octahedral perovskites: (1) geometrical constraints and (2) energetically favourable distortion.

Goldschmidt's principle—the radius ratio rule for the extended ionic lattice—is used to evaluate whether ABX_3 perovskites will form, postulating ranges governed by the ionic ratio of its sites[18–20]. The octahedral factor (μ) defines the ionic radii limits of the B and X sites for stabilization in the octahedral coordination (Fig. 1b). The ionic radii of coordinated sites should satisfy the condition $\sqrt{2}\ (r_B + r_X) < 2r_X$. When the

ionic radius of the metal centre (for example, Ge) is below the threshold (for example, 0.85 Å for iodide perovskite), the rigid spheres of X sites begin to collide with one another, destabilizing octahedral coordination (Fig. 1c)[21,22].

The Jahn–Teller (JT) effect contemplates the possibility of energy gain through spontaneous symmetry breaking in the condensed matter system[23]. The second-order JT instability, applied to the case of Ge with its low ionic radius and large energy gap between $4s$ and $4p$ orbitals (approximately 7 eV), leads to the s^* level of the resultant perovskites being lowered in energy, whereas triply degenerate p^* splits into two levels[17,24,25]. This breaking of orbital degeneracies leads to an electronic energy gain (that is, it widens the bandgap of germanium perovskites)[17,21,25,26].

From the analysis of previously published Ge-based perovskites (Extended Data Table 1), the B site departs from the centre to form three short (roughly 2.8 Å) and three long Ge–I bonds (roughly 3.3 Å), a layered geometry with a lower degree of B-site coordination than octahedral perovskites (Fig. 1d). In this way, the highest occupied

[1]The Edward S. Rogers Department of Electrical and Computer Engineering, University of Toronto, Toronto, Ontario, Canada. [2]Department of Physical and Environmental Sciences, University of Toronto Scarborough, Toronto, Ontario, Canada. [3]Department of Chemistry, University of Toronto, Toronto, Ontario, Canada. [4]Département de Chimie, Université de Montréal, Montréal, Québec, Canada. [5]Department of Chemistry, University of Victoria, Victoria, British Columbia, Canada. [6]Institut de Ciències Fotòniques, The Barcelona Institute of Science and Technology, Barcelona, Spain. ✉e-mail: ted.sargent@utoronto.ca
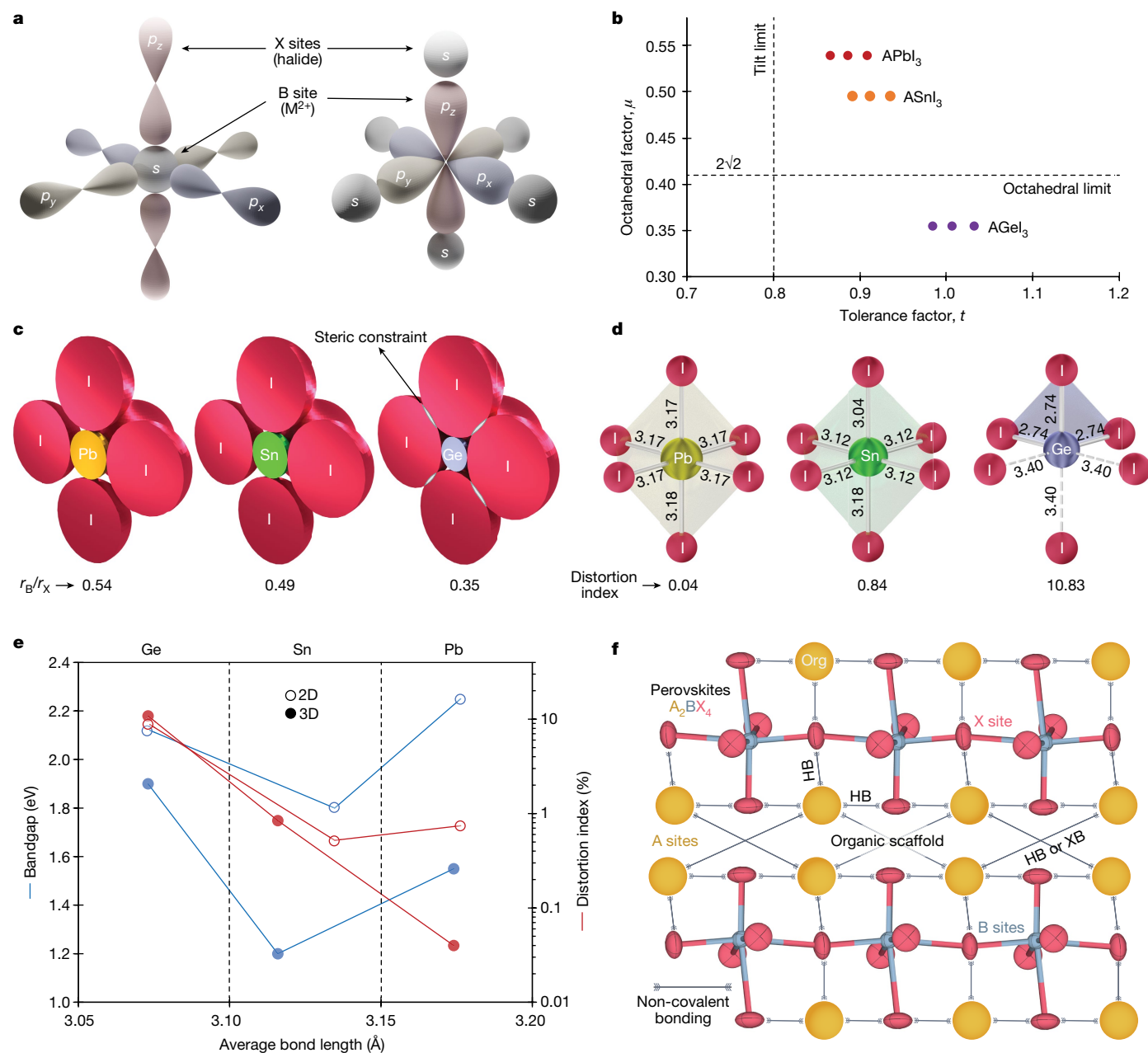
Fig. 1 | Distorted germanium perovskites. a, The main orbital character of valence ($s*$) and conduction ($p*$) bands of the perovskites for group IVa metal centre perovskites. **b**, Distribution of the perovskites (ABX_3) with Pb, Sn and Ge as the metal centre with respect to the limits of Goldschmidt octahedral and tolerance factor. Caesium, methylammonium and formamidinium are used as A sites for the calculation. **c**, Schematic representation of the octahedral limit for Ge perovskites compared with Pb and Sn perovskites. In the case of Ge, the assumed iodide spheres begin to collide with one another, which destabilizes the symmetric perovskite structure. **d**, Metal–iodide bond distances for Pb, Sn and Ge perovskites. The distances are obtained for the resolved perovskite structures with methylammonium as a cation. The calculated distortion indexes are indicated. **e**, The bandgap and distortion index of Pb, Sn and Ge perovskites are plotted in relation to their average bond distances. PEA and methylammonium are used as cations for the 2D and 3D perovskites, respectively. **f**, A concept representation of the organic scaffold as a supplementary crystal force that encloses the inorganic framework and reduces the octahedral distortion.

molecular orbital (HOMO) of the distorted MX_6 becomes s/p hybridized (that is, contribution of a lone pair of electrons to the valence band), resulting in the formation of polar trigonal pyramidal MX_3 units[2,17,25]. The accompanying large polarizability from this distortion has been harnessed for applications that require polar space groups, including ferroelectricity[27] and nonlinear optics[2].

Although the average bond distance (volume of virtual octahedral units) in Ge is lower than that in Pb and Sn, the bandgap of Ge perovskites is widened (Fig. 1e)–the result of the octahedral distortion–and

their diode performance lies below that of Pb and Sn perovskites[3]. Studies show that $CsGeX_3$, when subjected to high hydrostatic pressure, undergoes a reversible phase transition from the orthorhombic system (distorted octahedra) to the primitive cubic phase (symmetric octahedra)[17,21,25,26]. Pressure applied to Ge perovskites overcomes the geometrical strain and also, the electronic energy gain caused by distortion. This pressure progressively reduces the distortion and causes a decrease in bandgap at a high rate (−0.61 eV GPa^{-1} for $CsGeBr_3$).

Both Goldschmidt and JT analysis neglect bonding between A sites (cations) in perovskites, and this holds true in the case of three-dimensional (3D) perovskites. However, hybrid organic–inorganic perovskites open the prospect of non-covalent interaction between organics as an additional degree of freedom in design[28,29]. We postulated harnessing the chemical and structural versatility of organics to design supplementary crystal forces to stabilize octahedral perovskites.

Here, we sought to construct an organic scaffold inside perovskites that mimics the effect of external pressure and overcomes the geometrically and energetically favourable distortion (Fig. 1f). We would use synthons known from supramolecular chemistry[7,8], building blocks that rely on the hierarchy of non-covalent interactions to implement the main features of a crystal structure. Hydrogen bonding (HB) and halogen bonding (XB) are among the strongest and most versatile descriptors of supramolecular synthons for specific recognition[30,31]. These interactions also have been employed in perovskites to passivate defects, stabilize against moisture and tune interfacial energetic alignment[32–34].

We searched for self-complementary synthons to construct a functional scaffold. A wide variety of organic candidates—with aliphatic and aromatic backbones—were examined experimentally to test their capacity to form networks of intermolecular bonds (Fig. 2a). We explored functional groups that can form strong intermolecular bonds, focusing on HX and XB (Supplementary Note 1). Using single-crystal X-ray diffraction (XRD), the structures of 18 Ge perovskites were determined (Extended Data Table 2). In this study, we use the Baur distortion index (D_i) to quantify the asymmetry or distortion in the virtual octahedral unit of the perovskite crystal structure[35]:

$$D_i = \frac{1}{6} \sum_{i=1}^{6} \left(\frac{|b_i - \bar{b}|}{\bar{b}} \right),$$

where b_i and $\bar{b}$ are the individual Ge–I bond length and the average of six bond lengths, respectively. A higher distortion index corresponds to less symmetry within the octahedral units. We compare (Extended Data Fig. 1) the Baur distortion index with other metrics also used to quantify octahedral distortion. When the D_i exceeds 3% (as roughly estimated for Ge iodide perovskites) (Supplementary Note 2), the octahedral perovskite structures tend to distort into the polar non-perovskite structures with tetrahedral or trigonal pyramidal building blocks. Figure 2b shows the Ge–I bond lengths for the structures obtained and Fig. 2c visualizes the calculated distortion index of all resolved Ge perovskites so far. We summarize here.

1. Ge metal with inorganic (Cs) and relatively small organics (less than three carbons) forms 3D or one-dimensional perovskites with trigonal pyramidal units with $D_i > 4$% (P-2, P-9 to P-15, and P-18).
2. Organic molecules with aliphatic and aromatic backbones and no functional groups lead to polar perovskites with trigonal pyramidal and tetrahedral units with $D_i > 4$% (P-1, P-4, P-6, P-7, P-8, 1 and 13).
3. Aliphatic molecules with halogen functional groups form type II halogen bonds. These halogen bonds are isolated and do not create an extended network, resulting in the polar trigonal perovskites with $D_i > 8$% (crystal 15).
4. Organic molecules with two cationic sites form Dion–Jacobson-type perovskites. These Dion–Jacobson structures consist of mixed trigonal and octahedral units with D_i (average) of approximately 6.2% (crystal 14).
5. Organics with –CF$_3$, –OH and C–O–C functional groups form isolated (head-to-head) halogen or hydrogen bonds with an adjacent molecule from the opposite direction. These organics lead to polar perovskites with trigonal pyramidal units and $D_i > 5$% (crystals 6, 11, 16 and 17).
6. Organic molecules with phenylethylammonium (PEA) backbone and halogen (F, Cl and Br) in the *para*-position form XB and HB, but they still lead to the perovskite structure with $D_i > 8$% (P-3, P-5, 9 and 10).

7. Organic molecules with a backbone of phenylmethylammonium (PMA) and halogen (F, Cl, Br and I) in the *para*- and *meta*-positions form extended homomeric halogen and hydrogen bonds. These organic series lead to symmetric octahedral perovskites with $D_i < 0.45$% (crystals 2, 3, 4, 5, 7 and 8).

Since PMA haloorganics satisfy the requirements for scaffolding symmetric octahedral perovskites, we focus in on this series. In the case of H–PMA without halogen, the resulting perovskite adopts the zero-dimensional (0D) structure with mixed trigonal pyramidal and tetrahedral units. By contrast, perovskites with X–PMA cations with distinct acceptor and donor sites crystallize in the corner-sharing symmetric octahedral perovskite [GeI$_6$]$^{4-}$, a structure not allowed by Goldschmidt rules.

F–PMA crystallizes in a monoclinic perovskite with the organic modules aligned parallel to one other (Extended Data Figs. 2 and 3 and Supplementary Table 1). The hydrogen of the phenyl ring, having a partial positive charge (the nucleophile), is attracted electrostatically to the negative potential belt surrounding the C–F bond in the neighbouring molecule (electrophilic site), producing a network of bonding between A sites in the plane of perovskite growth (Fig. 3b). Other X–PMA molecules (X: Cl, Br and I) crystallize in an orthorhombic structure, with the molecules seated in an antiparallel fashion. The electron-poor σ-hole site at the halogen (XB donor) forms a short contact with the π-electron density of two carbons (XB acceptor) from the adjacent benzene ring[36] (Fig. 3c). This infinite chain of XB bonding displays a zigzag arrangement with an X...C*...X angle of 85.2°, with C* referring to the centroid of the double bond (Supplementary Note 3).

In cases of perovskites with X–PMA cations (X = Cl, Br, I) studied herein, there is a secondary sequence of non-covalent bonds antiparallel to the axis of the primary chain. The haloorganic molecules are bent and seated at an angle of 45° with respect to the plane of the inorganic framework. In this fashion, the hydrogen of the phenyl ring makes a hydrogen bond with the negative potential belt of iodide in the inorganic framework (Extended Data Figs. 4 and 5). This two-dimensional (2D) skeleton of extended strong intermolecular bonding provides stabilization of the symmetric octahedral perovskite structure with a short Ge–I bonding distance.

Both XB and HB provide nearly linear interactions between a nucleophile and an electrophilic site, with the latter located on the terminus of either a hydrogen (in HB) or halogen atom (in XB) that is bonded to an electron-withdrawing group. In the benzene ring, wherein the halogen atom is involved, there is a region with positive potential at the terminus of the C–X bond (the σ hole), and this is surrounded by a belt of negative potential orthogonal to the covalent bond (Fig. 3a). The σ hole becomes larger as the size of the halogen increases (from F to I). Consequently, fluorine is more susceptible to HB from the negative belt of the C–F bond, while iodide makes the strongest XB at the elongation of the C–I bond (Fig. 3d).

Powder XRD shows that the perovskite interlayer spacing increases from 13 Å for (PMA)$_2$GeI$_4$ to 17 Å for (Br–PMA)$_2$GeI$_4$ (Fig. 4a). (PMA)$_2$GeI$_4$ has an indirect bandgap, while (Br–PMA)$_2$GeI$_4$ has a direct bandgap and is redshifted by approximately 0.5 eV, reaching 680 nm (Fig. 4b). The Pb-based perovskites (2D and 3D) are highly symmetric, with a distortion index close to zero (less than 1%). By contrast, the D_i for Ge-based perovskites exceeds 5%, which indicates significant asymmetry in the octahedra due to the large deviation in Ge–XB distance. When we employ HX and HB networks in the Ge perovskite framework, we instead observe D_i comparable with or even smaller (less than 0.4%) than the analogous Pb-based perovskites (Fig. 4c).

The bandgap of organic 2D perovskites depends on the interlayer spacing and metal–halogen–metal bonding angle[37]. However, these factors alone do not allow us to explain the significant redshift in the bandgap of Ge perovskite. Indeed, the trend of redshift with increasing interlayer spacing is contrary to what is expected (Fig. 4d).
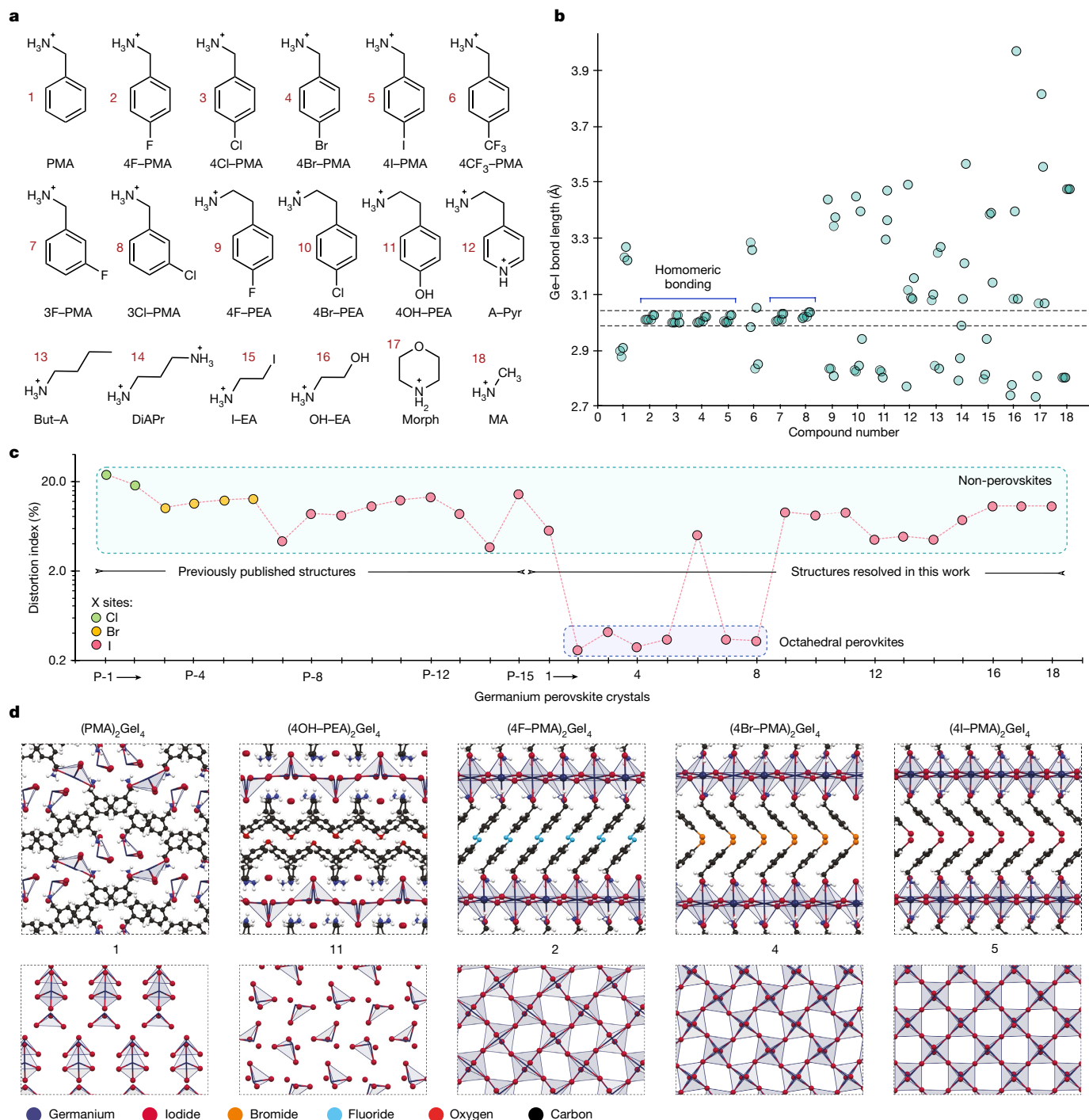
Fig. 2 | Ge perovskites having a symmetric octahedral structure. a, Organics used as cations for Ge perovskites. Each organic has been assigned a compound number and abbreviation. **b**, Ge–I bond lengths of perovskites synthesized herein; the molecules are identified in **a**. Details are in Extended Data Table 2 as well as Supplementary Figs. 1–15 and Supplementary Table 1. **c**, Distortion index for previously published Ge perovskite structures (P-1 to P-15) along with the resolved structures in this study (1–18). Perovskites with distortion indexes below 0.5% have symmetric octahedra. **d**, Germanium perovskite crystal structure resolved by single-crystal XRD viewed along two different crystallographic axes for the perovskite crystals 1, 11, 2, 4 and 5. Organic molecules are omitted in the lower panels.

Whether octahedral deformation modes in Ge perovskites are primarily enforced by electronic instability or semiclassical geometrical constraints, the fingerprint of JT distortion (3 + 3 splitting) has been observed in numerous Ge perovskite crystals with the stereochemical expression of a lone pair in Ge (Fig. 2b). The M–X nearest-neighbour interactions (s bonds) are the largest contributors to the overall energy in perovskites and determine the frontier band energies. In general, the A-site cation has no significant electronic interaction with the M–X sublattice and does not contribute meaningfully to the electronic structure near the band edges. However, here we show that the organic sublattice network is capable of transforming the electronic configuration of crystals while preserving the conduction and valence bands localized on the inorganic framework (Fig. 4i,j).
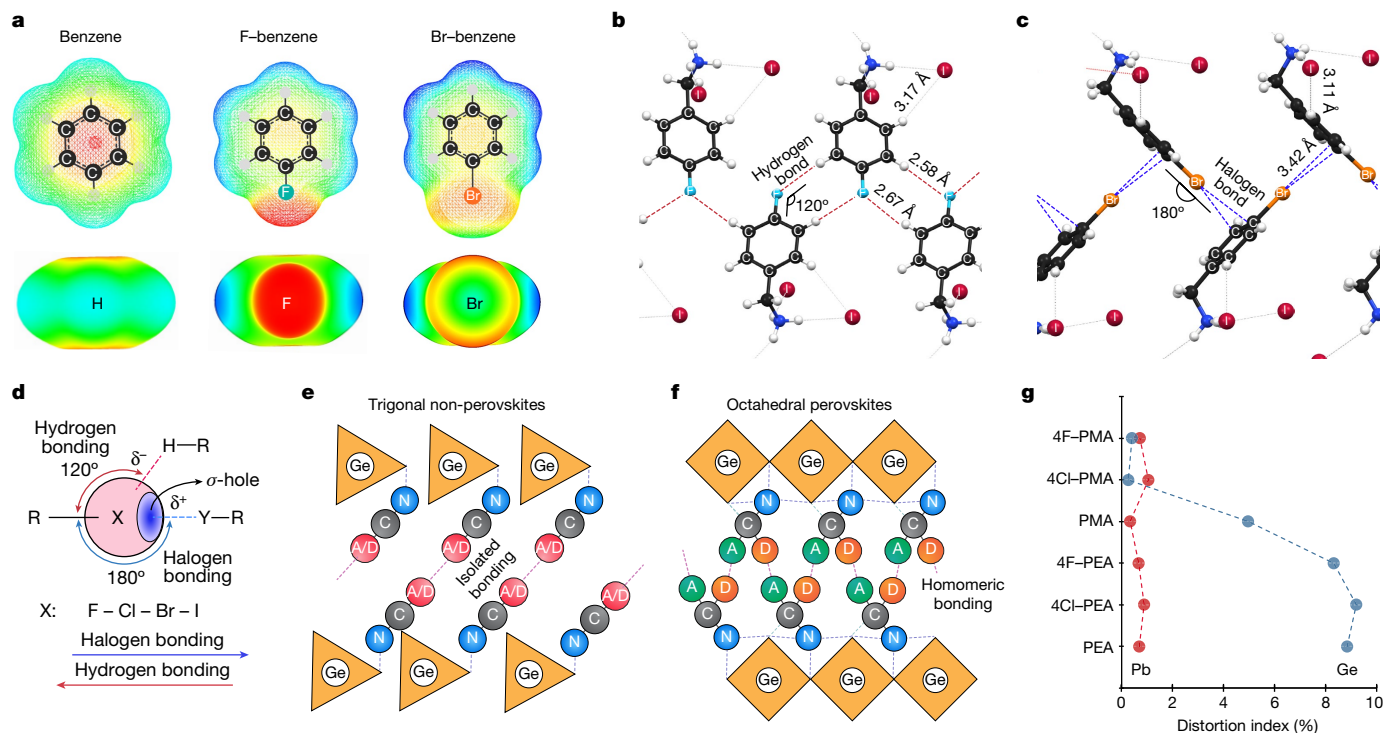
Fig. 3 | Hydrogen and halogen intermolecular bonding as crystal forces.
a, DFT-calculated molecular electrostatic potential perpendicular to the benzene ring and along the axis of the halogen–benzene bond for H–PMA, F–PMA and Br–PMA. **b**, Network of HB in the crystal structure of Ge perovskites with F–PMA as cations. The extended network of the HB, between the F atom and the H atom of the neighbouring benzene ring, is shown by the red dashed lines. **c**, Network of XB in the crystal structure of Ge perovskites with Br–PMA as cations. The extended zigzag network of the XB bonding, between the Br atom and π electrons of the neighbouring benzene ring, is shown by the blue dashed lines. **d**, Schematic representation of directionality and bonding angle model for HB and XB. The type and strength of the intermolecular bonding are dependent on the halogen atoms. **e,f**, Scenarios for the organics capable of making intermolecular bonding in the case of head-to-head isolated bonding between organics (**e**) and formation of a homomeric network of bonding between organic modules (**f**). **g**, Distortion index for the Pb and Ge perovskites with a backbone of PEA and PMA.

The organic sublattice, intricately interconnected by homomeric non-covalent bonds, influences the complex geometry of the inorganic framework via its strong interactions with X sites (anions). In a simple view of a symmetry-adapted linear combination of atomic orbitals, the imposed directionality and symmetric arrangement of atomic orbitals in the inorganic sublattice lead to strong orbital hybridization that diminishes the localization of degenerate states needed for JT distortion. In crystals containing organic scaffolds, the bandgap shrinkage reflects this strong hybridization. In this scenario, the energy gained by electronic degeneracy removal may be too weak to enforce second-order Jahn–Teller (SOJT) distortion.

We carried out density functional theory (DFT) simulations (Fig. 4e) and observed the evolution from indirect to direct optical transition upon the formation of symmetric GeI_6 octahedra (Fig. 4f,g). DFT also indicates a significant decrease in the electron and hole effective masses (approximately 10×) from PMA to PMA–X cation-based germanium perovskites (Fig. 4h). The calculated charge mapping density of $(4Br–PMA)_2GeI_4$, shown in Fig. 4j, demonstrates that organic cations do not contribute to the frontier band structures. The near-spherical and symmetric Ge's charge density suggests that the s/p hybridization of Ge orbitals is suppressed, and there is no contribution of the Ge p orbital to valence band maximum. The partial density of states further supports this conclusion (Supplementary Fig. 17). Further, it indicates that the Ge p orbital interacts with both the s and p orbitals of iodide to create p^* at the bottom of the conduction band with an approximately 1 eV downshift compared with the crystal with PMA cation.

It should be noted that homomeric bonding not only minimizes structural distortion but also reduces the virtual octahedral volume. For instance, $(4I–PMA)_2GeI_4$ has approximately 12 and 10% lower octahedral volumes compared with 3D (methylammonium as a cation) and 2D (PEA as a cation) Ge perovskites, respectively. This reduction in octahedral volume can be a contributing factor in the observed redshift in the bandgap. Indeed, the scaffold construction that enfolds the inorganic framework simulates the effect of external hydrostatic pressure to stabilize symmetric octahedral Ge perovskites (Fig. 1f). This organic scaffold overcomes steric constraints and removes the energetically favourable distortion. Later, we demonstrate the application of this strategy to quasi-2D systems.

We summarize by offering these guidelines for the creation of an extended network (scaffold) of organics inside perovskites. (1) The organic modules must include the functional group capable of forming intermolecular bonds (Fig. 3e). Halogen atoms meet this requirement. (2) The organic modules should be self-complementary and bear both acceptor and donor sites. In this case, the bonding is extended and forms a homomeric scaffold (Fig. 3f). The π electrons in the benzene ring can be used as an acceptor for XB. (3) Organic molecules should possess a high degree of rigidity to limit the possibility of different bonding configurations (particularly the expanded version). Figure 3g shows that PEA opposed to PMA as an organic backbone renders the expanded homomeric bonding (both XB and HB) ineffective (weak) for scaffolding the symmetric octahedral perovskites. It is intended that the ammonium tails of organic backbones have a minimum number of sp^3-hybridized carbons.

It is worth noting that crystal structures are emergent properties and evolve from a combination of chemistry and geometry. The criteria we have outlined may serve as a minimum requirement for the extension of homomeric bonding in perovskites. In Extended Data Fig. 8, we
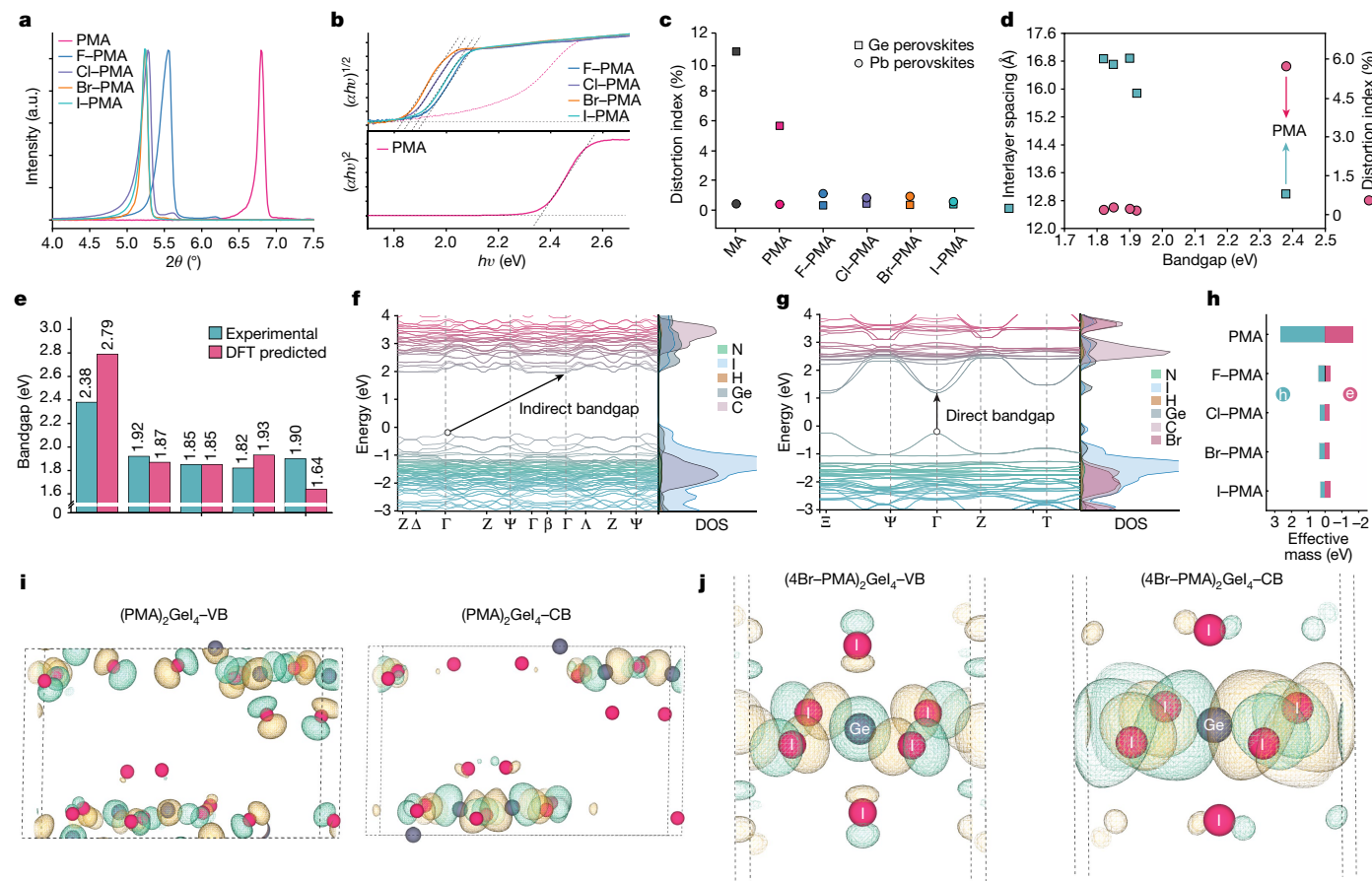
Fig. 4 | Effect of intermolecular bonding on perovskite properties. a, First peak in the powder XRD (P-XRD) pattern for the Ge perovskites with indicated cations. Data have been collected on the powder samples. Supplementary Fig. 16 has a wider range of P-XRD patterns. a.u., arbitrary units. **b**, Tauc plot to determine the bandgap for (1) direct and (2) indirect allowed optical transitions. **c**, Octahedral distortion index (D_i) comparison between Pb and Ge perovskites for a range of cations. The structures of molecules are shown in Fig. 2a. Square and circle markers represent Ge and Pb perovskites, respectively. **d**, Plot of the interlayer spacing and distortion index versus bandgap for the Ge perovskites shown in **a** and **b**. **e**, Comparison between experimentally measured and theoretically estimated bandgap for a range of Ge perovskites. A plane-wave basis set with a Perdew–Burke–Ernzerhof functional has been used for the DFT calculations. **f,g**, Calculated electronic band structure and atomic orbital projected density of states (DOS) of the Ge perovskite with PMA (**f**) and Br–PMA (**g**) as cations (Extended Data Fig. 6 shows the electronic band structure of remaining crystals). **h**, Calculated effective electron and hole mass for a range of Ge perovskites. **i,j**, Charge density mapping of the conduction band (CB) and valence band (VB) in the Ge perovskite with PMA (**i**) and Br–PMA (**j**) as cations. Note that for both cases, the contribution of the DOS on the organic parts is negligible, and thus, organic molecules are not shown in the figure (Extended Data Fig. 7 shows the charge density mapping of the remaining crystal structures). MA, methylammonium.

provide examples that satisfy these criteria for extended bonding and show desired packing with a homomeric chain.

We aimed to determine whether the formation of an organic sublattice is unique to Ge perovskites or whether it can also impact perovskites employing other metals also having low ionic radii. To this end, we studied copper (Cu), a transition metal whose atomic orbital configurations differ from those of p-block metals, such as Pb and Ge. Cu^{2+} with an electronic configuration of [Ar] $3d^9$ often results in the formation of distorted perovskites with square planar structures, as evidenced by the [$CuCl_4$] polyhedron (Supplementary Fig. 18a–d). We found that homomeric bonding induces a transformation of Cu perovskites into octahedral structures (Supplementary Fig. 18e). The virtual octahedral volume for Cu perovskites was found to be approximately 20% smaller than that of Ge perovskites. In these densely packed structures, other intermolecular interactions, including π–π stacking, become effective in establishing the homomeric bond chains.

We fabricated semiconductor diode devices using Ge-based and Pb-based active layers as controls (Fig. 5a). The hole and electron transport layers were composed of PEDOT:PSS and C_{60}/BCP, respectively. The use of X–PMA resulted in high-quality films, while H–PMA cations did not produce smooth films or performing devices, showing negligible photoresponse. The Ge perovskite with F–PMA cation showed a large redshift (approximately 0.5 eV) in the bandgap compared with its Pb analogue. Devices with Ge perovskite had an external quantum efficiency (EQE) of 23% at around 600 nm, while devices with Pb perovskite had an EQE of 18% at 480 nm (Fig. 5b). The current–voltage curve under illumination also indicated higher short-circuit current density (J_{sc}) and open-circuit voltage (V_{oc}) for 2D Ge perovskite compared with Pb (Fig. 5c).

To understand the impact of intermolecular interactions on the inorganic framework in a quasi-2D system, we synthesized a Ge perovskite with Cs and Cl–PMA cations, with $n = 2$ quantum wells. The single-crystal XRD of Cs(Cl–PMA)$_2$Ge$_2$I$_7$, as shown in Fig. 5d, indicated that the network of XB influences the Ge–I bond distance and symmetry factors in the inorganic octahedra. The organic scaffold was strong enough to reduce the distortion of the octahedral units by more than seven times compared with its 3D analogue (Fig. 5e).

We evaluated the performance of Ge perovskites in quasi-2D systems, aiming to combine the benefits of the symmetric octahedra of the engineered 2D structure with the reduced bandgap of 3D perovskites.
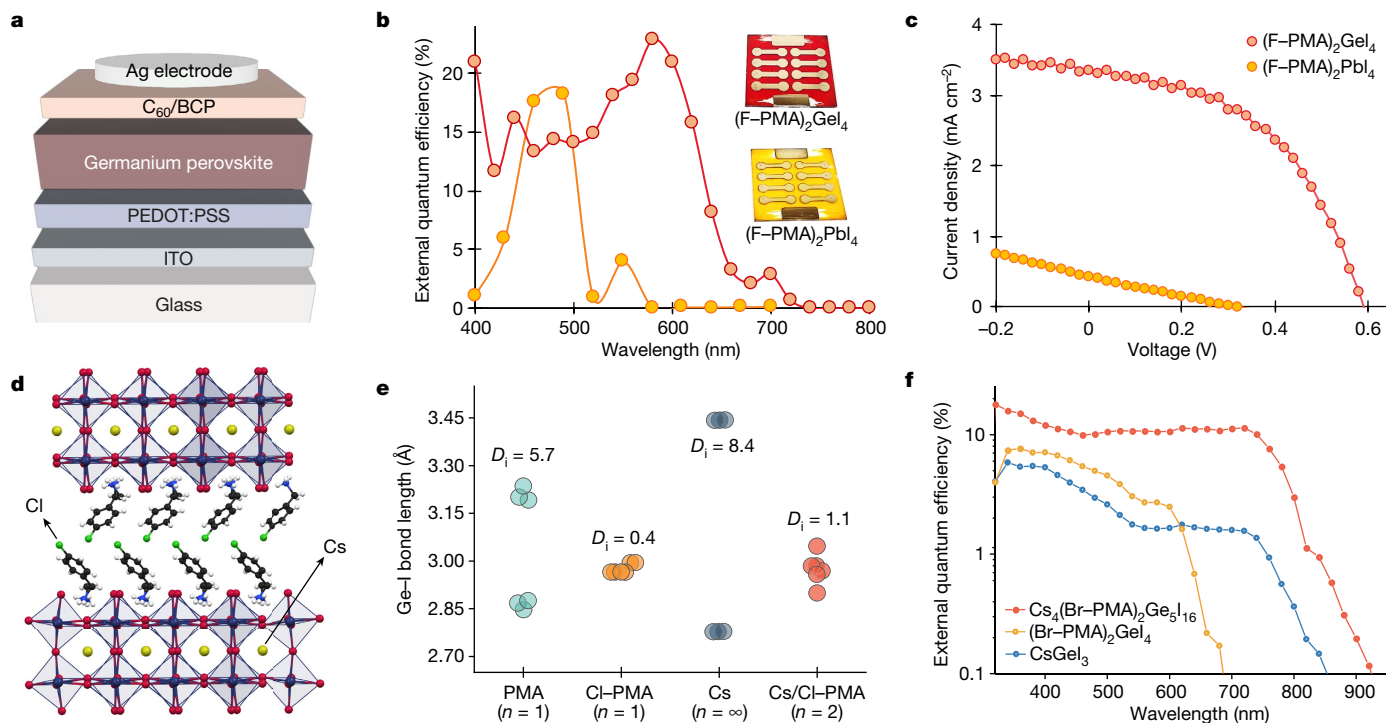
Fig. 5 | Photodiode studies and crystal structures of quasi-2D Ge perovskite. **a**, Architecture of p–i–n photodiodes. **b**, EQE of photodiodes fabricated using 2D Ge- and Pb-based perovskites. The insets show the optical images of devices. **c**, Illuminated current–voltage plot of the devices shown in **b**. **d**, Crystal structure of quasi-2D Ge perovskite with composition $Cs(Cl–PMA)_2Ge_2I_7$. **e**, Ge–I bond length in the 2D, 3D and quasi-2D systems. The octahedral distortion index (D_i) is indicated on the graph for each case. **f**, EQE of photodiodes as a function of active layer.

Devices with 2D perovskites using Cl–PMA cation showed an EQE of around 8% at 350 nm. Devices with 3D perovskites utilizing Cs as a cation had a low EQE of 2% at 750 nm. The quasi-2D perovskite using a mixture of Cs and Cl–PMA cations (with a mixing ratio for $n = 5$ quantum wells) showed significant improvement over both its 2D and 3D counterparts, with an EQE of 12% at 750 nm.

The strategy reported herein enables octahedral perovskites beyond what is postulated in Goldschmidt's rule. It focuses on the design of connected organic sublattices via the molecular design of self-complementary synthons, enabling control over the electronic and bonding configuration of inorganic frameworks. We report as a result control over JT distortion with implications in materials potentially spanning magnetism, ferroelectricity, photocatalysis and superconductivity. For future studies, it will be of interest to investigate the dynamics of crystallization; this will clarify whether intermolecular bonds are a postnucleation effect that alters structure at later stages of growth or whether organic scaffolds create the initial template for crystallization.

Online content

Any methods, additional references, Nature Portfolio reporting summaries, source data, extended data, supplementary information, acknowledgements, peer review information; details of author contributions and competing interests; and statements of data and code availability are available at https://doi.org/10.1038/s41586-023-06209-y.

1. Chiara, R., Morana, M. & Malavasi, L. Germanium-based halide perovskites: materials, properties, and applications. *Chempluschem* **86**, 879–888 (2021).
2. Stoumpos, C. C. et al. Hybrid germanium iodide perovskite semiconductors: active lone pairs, structural distortions, direct and indirect energy gaps, and strong nonlinear optical properties. *J. Am. Chem. Soc.* **137**, 6804–6819 (2015).
3. Ke, W. & Kanatzidis, M. G. Prospects for low-toxicity lead-free perovskite solar cells. *Nat. Commun.* **10**, 965 (2019).
4. Chen, M. et al. Highly stable and efficient all-inorganic lead-free perovskite solar cells with native-oxide passivation. *Nat. Commun.* **10**, 16 (2019).
5. Glück, N. & Bein, T. Prospects of lead-free perovskite-inspired materials for photovoltaic applications. *Energy Environ. Sci.* **13**, 4691–4716 (2020).
6. Xiao, Z., Song, Z. & Yan, Y. From lead halide perovskites to lead-free metal halide perovskites and perovskite derivatives. *Adv. Mater.* **31**, 1803792 (2019).
7. Desiraju, G. R. Crystal engineering: from molecule to crystal. *J. Am. Chem. Soc.* **135**, 9952–9967 (2013).
8. Mukherjee, A. Building upon supramolecular synthons: some aspects of crystal engineering. *Cryst. Growth Des.* **15**, 3076–3085 (2015).
9. Fu, Y. et al. Metal halide perovskite nanostructures for optoelectronic applications and the study of physical properties. *Nat Rev Mater* **4**, 169–188 (2019).
10. Nayak, P. K., Mahesh, S., Snaith, H. J. & Cahen, D. Photovoltaic solar cell technologies: analysing the state of the art. *Nat Rev Mater* **4**, 269–285 (2019).
11. Kim, J. Y., Lee, J. W., Jung, H. S., Shin, H. & Park, N. G. High-efficiency perovskite solar cells. *Chem. Rev.* **120**, 7867–7918 (2020).
12. Kojima, A., Teshima, K., Shirai, Y. & Miyasaka, T. Organometal halide perovskites as visible-light sensitizers for photovoltaic cells. *J. Am. Chem. Soc.* **131**, 6050–6051 (2009).
13. Hailegnaw, B., Kirmayer, S., Edri, E., Hodes, G. & Cahen, D. Rain on methylammonium lead iodide based perovskites: possible environmental effects of perovskite solar cells. *J. Phys. Chem. Lett.* **6**, 1543–1547 (2015).
14. Babayigit, A., Ethirajan, A., Muller, M. & Conings, B. Toxicity of organometal halide perovskite solar cells. *Nat. Mater.* **15**, 247–251 (2016).
15. Siebentritt, S. et al. Heavy alkali treatment of Cu(In,Ga)Se₂ solar cells: surface versus bulk effects. *Adv. Energy Mater.* **10**, 1903752 (2020).
16. Hoye, R. L. Z. et al. Fundamental carrier lifetime exceeding 1 μs in Cs₂AgBiBr₆ double perovskite. *Adv. Mater. Interfaces* **5**, 1800464 (2018).
17. Seo, D. K., Gupta, N., Whangbo, M. H., Hillebrecht, H. & Thiele, G. Pressure-induced changes in the structure and band gap of CsGeX₃ (X=Cl, Br) studied by electronic band structure calculations. *Inorg. Chem.* **37**, 407–410 (1998).
18. Filip, M. R. & Giustino, F. The geometric blueprint of perovskites. *Proc. Natl Acad. Sci. USA* **115**, 5397–5402 (2018).
19. Li, X. et al. Tolerance factor for stabilizing 3D hybrid halide perovskitoids using linear diammonium cations. *J. Am. Chem. Soc.* **144**, 3902–3912 (2022).
20. Fedorovskiy, A. E., Drigo, N. A. & Nazeeruddin, M. K. The role of Goldschmidt's tolerance factor in the formation of A₂BX₆ double halide perovskites and its optimal range. *Small Methods* **4**, 1900426 (2020).
21. Yamada, K., Mikawa, K., Okuda, T. & Knight, K. S. Static and dynamic structures of CD₃ND₃GeCl₃ studied by TOF high resolution neutron powder diffraction and solid state NMR. *J. Chem. Soc. Dalton Trans.* **10**, 2112–2118 (2002).
22. Yamada, K. et al. Structural phase transitions of the polymorphs of CsSnI₃ by means of Rietveld analysis of the X-ray diffraction. *Chem. Lett.* **20**, 801–804 (1991).
23. Varignon, J., Bibes, M. & Zunger, A. Origins versus fingerprints of the Jahn–Teller effect in d-electron ABX3 perovskites. *Phys Rev Res* **1**, 033131 (2019).
24. Albright, T. A., Burdett, J. K. & Whangbo, M. H. *Orbital Interactions in Chemistry*. 2nd edn (Wiley, 2013).

25. Schwarz, U., Wagner, F., Syassen, K. & Hillebrecht, H. Effect of pressure on the optical-absorption edges of $CsGeBr_3$ and $CsGeCl_3$. *Phys. Rev. B Condens. Matter Mater. Phys.* **53**, 12545–12548 (1996).

26. Thiele, G., Rotter, H. W. & Schmidt, K. D. Kristallstrukturen und Phasentransformationen von Caesiumtrihalogenogermanaten(II) $CsGeX_3$ (X = Cl, Br, I). *ZAAC J. Inorg. Gen. Chem.* **545**, 148–156 (1987).

27. Christensen, A. N. et al. A ferroelectric chloride of perowskite type crystal structure of $CsGeCl_3$. *Acta Chem. Scand.* **19**, 421–428 (1965).

28. Saparov, B. & Mitzi, D. B. Organic-inorganic perovskites: structural versatility for functional materials design. *Chem. Rev.* **116**, 4558–4596 (2016).

29. Jana, M. K. et al. Structural descriptor for enhanced spin-splitting in 2D hybrid perovskites. *Nat. Commun.* **12**, 4982 (2021).

30. Cavallo, G. et al. The halogen bond. *Chem. Rev.* **116**, 2478–2601 (2016).

31. Varadwaj, P. R., Varadwaj, A. & Marques, H. M. Halogen bonding: a halogen-centered noncovalent interaction yet to be understood. *Inorganics (Basel)* **7**, 40 (2019).

32. Metrangolo, P., Canil, L., Abate, A., Terraneo, G. & Cavallo, G. Halogen bonding in perovskite solar cells: a new tool for improving solar energy conversion. *Angew. Chem. Int. Ed. Engl.* **61**, e202114793 (2022).

33. Ball, M. L., Milic, J. V. & Loo, Y. L. The emerging role of halogen bonding in hybrid perovskite photovoltaics. *Chem. Mater.* **23**, 8 (2021).

34. Fu, X. et al. Halogen-halogen bonds enable improved long-term operational stability of mixed-halide perovskite photovoltaics. *Chem* **7**, 3131–3143 (2021).

35. Baur, W. H. The geometry of polyhedral distortions. Predictive relationships for the phosphate group. *Acta Crystallogr. B* **30**, 1195–1215 (1974).

36. Baldrighi, M. et al. Polymorphs and co-crystals of haloprogin: an antifungal agent. *CrystEngComm* **16**, 5897–5904 (2014).

37. Wang, P. X. et al. Structural distortion and bandgap increase of two-dimensional perovskites induced by trifluoromethyl substitution on spacer cations. *J. Phys. Chem. Lett.* **11**, 10144–10149 (2020).

Methods

Materials and preparation

GeO_2 (99.999%), 4-fluorobenzylamine (97%), 4-bromobenzylamine (96%), 4-chlorobenzylamine (98%), 4-iodobenzylamine, hydriodic acid (57 wt% in H_2O, 99.95%), hypophosphorous acid solution (50 wt% in H_2O), toluene (99.5%), N,N-dimethylformamide (anhydrous, 99.8%), CsI (99.95%) and dimethyl sulfoxide (anhydrous, 99.9%) were purchased from Sigma-Aldrich and used as received. Methylammonium iodide (greater than 99.99%) was purchased from Greatcell Solar Materials.

Perovskite synthesis

We prepared GeI_2 stock solution using GeO_2 (0.4 mM) and mixed solvent of hydriodic acid (70%) and hypophosphorous acid (30%) at approximately 390 K (using sealed 20-ml vials and a hot plate). Stock solutions of GeI_2 were mixed with candidate organic precursors (ammonium salts or amine) at the stoichiometric ratio (2× molarity of GeI_2). The temperature of the mixed solution was raised to 390 K while stirring for approximately 1.5 h. In the case that organic salts were not dissolved, minimum hydroiodic acid (mixed with hypophosphorous acid) was added until the salts had been completely dissolved. It should be noted that some perovskite candidates require five times the amount of initial acid to dissolve completely. Once dissolved, the system was allowed to cool passively to room temperature to yield yellow to dark brown 2D germanium perovskite crystals. These crystals were collected by vacuum filtration, washed three times with toluene and dried under a vacuum overnight. The crystals were kept in a vacuum chamber until usage. Quasi-2D perovskites were synthesized following the same procedure as described above with a stoichiometric amount of the cations added to the solution, resulting in the formation of the corresponding compound. We note that the Ge perovskites are susceptible to being spontaneously oxidized in the air. After one night in a vacuum, we transferred the samples to a nitrogen glove box. The crystals were vacuum sealed inside the N_2 glove box until further analysis.

Device fabrication

Indium tin oxide (ITO) electrode on glass substrates were washed using an ultrasonic bath in acetone, water and isopropanol (40 min each). The PEDOT:PSS (Xi'an PLT) solution was filtered using a 0.45-μm syringe filter and was spin coated on the cleaned substrate at 4,000 rpm for 30 s followed by annealing at 150 °C on a hot plate for 40 min in ambient air. The substrates were transferred to a nitrogen-filled glove box. For the deposition of the perovskite films, the corresponding synthesized perovskites crystals were dissolved in a mixture solution of dimethylformamide:dimethylsulfoxide (3:1) at the concentration of 0.5 M. After stirring at room temperature for 30 min, the solution was filtered through a 0.45-μm polytetrafluoroethylene (PTFE) syringe filter. The prepared solution was spin coated on the glass/ITO/PEDOT:PSS substrates in a two-step procedure: (1) 1,000 rpm for 10 s with a ramping speed of 200 rpm s^{-1} and (2) 4,000 rpm for 50 s with an acceleration of 1,000 rpm s^{-1}. During the second spin-coating step, 250 μl of chlorobenzene (anhydrous, 99.8%) was dispensed dynamically on the substrate at 25 s before the end of the procedure. Immediately after deposition, the substrates were annealed on a hot plate at 100 °C for 10 min. C_{60} (Xi'an PLT), BCP (TCI Chemicals) and Ag electrodes were deposited in an angstrom thermal evaporation system to form 20 nm C_{60}, 7 nm bathocuproine (BCP) and 250 nm Ag on top of the perovskite layer, respectively. Until further characterization, the samples were kept in an N_2 glove box. The data points in Fig. 5b,c,f represent the average of six pixels.

Characterization

Powder XRD patterns were collected on a Rigaku MiniFlex 600 6G Benchtop powder XRD instrument using Cu Kα radiation (λ = 1.5406 Å).

Reported P-XRD patterns are collected for powder samples. Ultraviolet–visible absorption spectroscopy was performed on a PerkinElmer LAMBDA 950 spectrophotometer and universal integrating sphere. Power samples were sandwiched between two pieces of glass for absorption measurements. Single-crystal XRD analysis for crystal numbers 1, 2, 3, 4, 5, 7, 8, 9, 11, 14, 15, 16 and 18 were obtained on a Bruker Kappa APEX-DUO CCD Diffractometer (Mo Kα with λ = 0.71073 Å and Cu Kα with λ = 1.54178 Å). The data for crystal numbers 12, 13 and 17 were collected from a shock-cooled single crystal at 150 K on a Bruker Venture Metaljet κ-geometry diffractometer with a Metal Jet using a Helios MX Mirror Optics as monochromator and a Bruker CMOS Photon III detector. The diffractometer was equipped with an Oxford Cryostream 700 low-temperature device and used Ga K_{α} radiation (λ = 1.34139 Å). All data were integrated with SAINT (2020), and a multi-scan absorption correction using SADABS 2016/2 was applied. The structure was solved by dual methods with XT and refined by full-matrix least-squares methods against F^2 using XL. All non-hydrogen atoms were refined with anisotropic displacement parameters. The hydrogen atoms were refined isotropically on calculated positions using a riding model with their isotropic displacement parameter (U_{iso}) values constrained to 1.5 times the equivalent displacement parameter (U_{eq}) of their pivot atoms for terminal sp^3 carbon atoms and 1.2 times for all other atoms. The responsivity and quantum efficiency of the photodiodes were measured using a QUANTX-300 Newport measurement system. No external bias was applied, and measurements were taken under constant nitrogen flow. A standard calibrated Si/Ge reference detector (BD005, Newport) was used to calibrate the system over the wavelength range from 350 to 1,800 nm. Calibration was conducted before each set of measurements to create the reference values. A silicon photovoltaic test cell was used to further validate the calibration procedure.

Theoretical calculations

DFT calculations were performed using the Vienna Ab Initio Simulation Package[38,39] employing a plane-wave basis set with a Perdew–Burke–Ernzerhof functional[40]. The projector-augmented wave method[41] was used to solve the ion–electron interactions in the periodic system. Structural data were obtained from experimental XRD results. The Monkhorst–Pack k-points mesh with a Kmesh-resolved value of 0.04 2π Å^{-1} was utilized[42]. For the calculation of bandgaps, a hybrid functional (HSE06) was used with the default value of AEXX = 0.25 (ref. 43).

Data availability

Crystallographic data for the structures reported in this article have also been deposited at the Cambridge Crystallographic Data Centre, with deposition numbers indicated in the Supplementary Information. Data are also available on request.

38. Kresse, G. & Furthmüller, J. Efficiency of ab-initio total energy calculations for metals and semiconductors using a plane-wave basis set. *Comput. Mater. Sci.* **6**, 15–50 (1996).
39. Kresse, G. & Hafner, J. Ab initio molecular dynamics for liquid metals. *Phys. Rev. B* **47**, 558–561 (1993).
40. Perdew, J. P., Burke, K. & Ernzerhof, M. Generalized gradient approximation made simple. *Phys. Rev. Lett.* **77**, 3865–3868 (1996).
41. Payne, M. C., Teter, M. P., Allan, D. C., Arias, T. A. & Joannopoulos, J. D. Iterative minimization techniques for ab initio total-energy calculations: molecular dynamics and conjugate gradients. *Rev. Mod. Phys.* **64**, 1045–1097 (1992).
42. Monkhorst, H. J. & Pack, J. D. Special points for Brillouin-zone integrations. *Phys. Rev. B* **13**, 5188–5192 (1976).
43. Krukau, A. V., Vydrov, O. A., Izmaylov, A. F. & Scuseria, G. E. Influence of the exchange screening parameter on the performance of screened hybrid functionals. *J. Chem. Phys.* **125**, 5029 (2006).

Article

Extended Data Fig. 1 | Comparison of different metrics for the quantification of octahedral distortion. A plot of Baur distortion index *vs* **a**, Bond angle variance **b**, Quadratic elongation **c**, Effective coordination number **d**, Bond distortion (Δd) **e**, Polyhedral volume **f**, Average bong length. Octahedral perovskites are identified by the yellow circles in each graph. See Supplementary note 4 for the definition of each metric.

Article

a

| b-c axis | a-c axis | a-b axis |

b

| b-c axis | a-c axis | a-b axis |

c

| b-c axis | a-c axis | a-b axis |
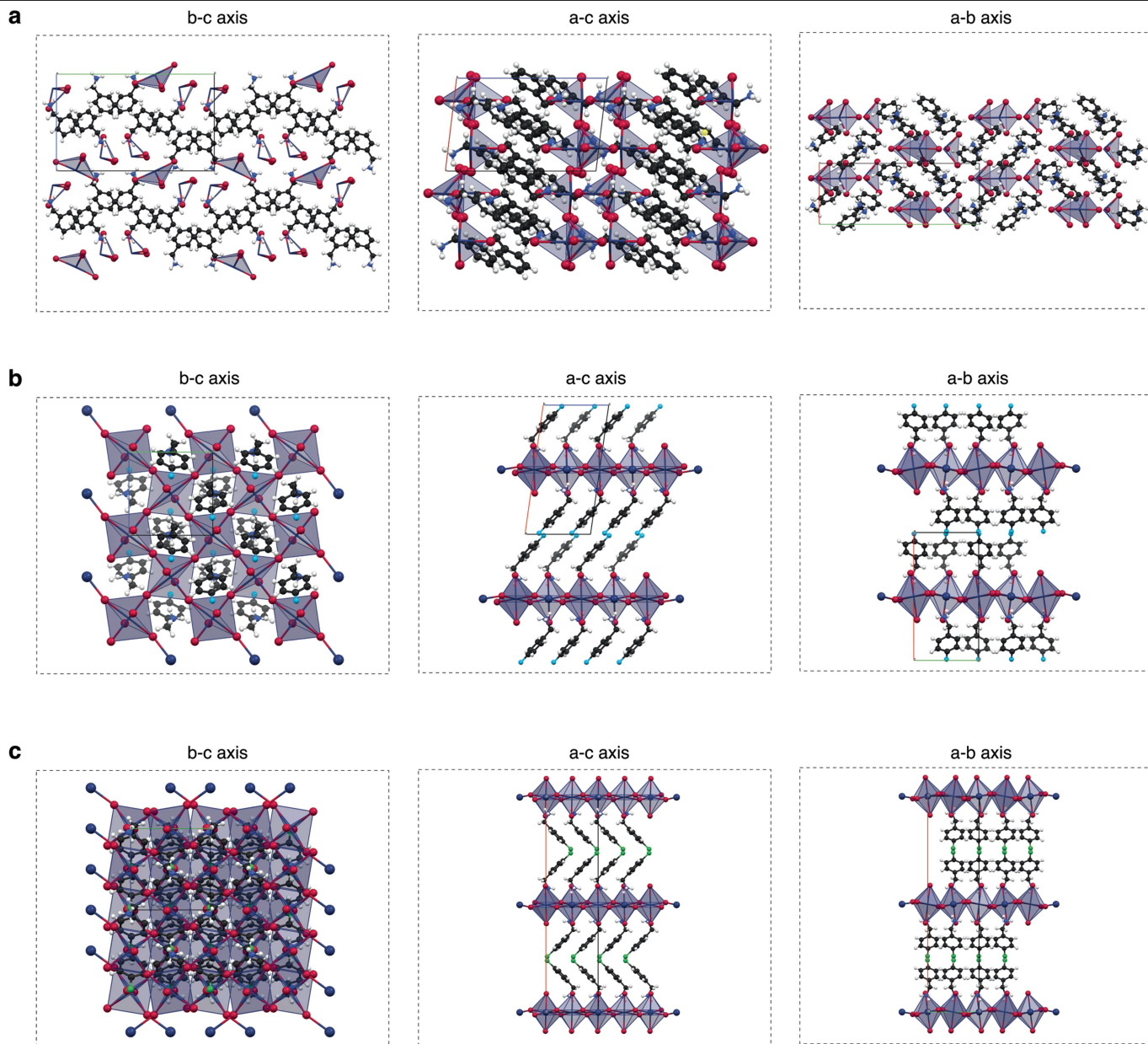
Extended Data Fig. 2 | Crystal structure of a. $(PMA)_2GeI_4$; **b**, $(4F\text{-}PMA)_2GeI_4$; **c**, $(4Cl\text{-}PMA)_2GeI_4$ with indicated view axis.
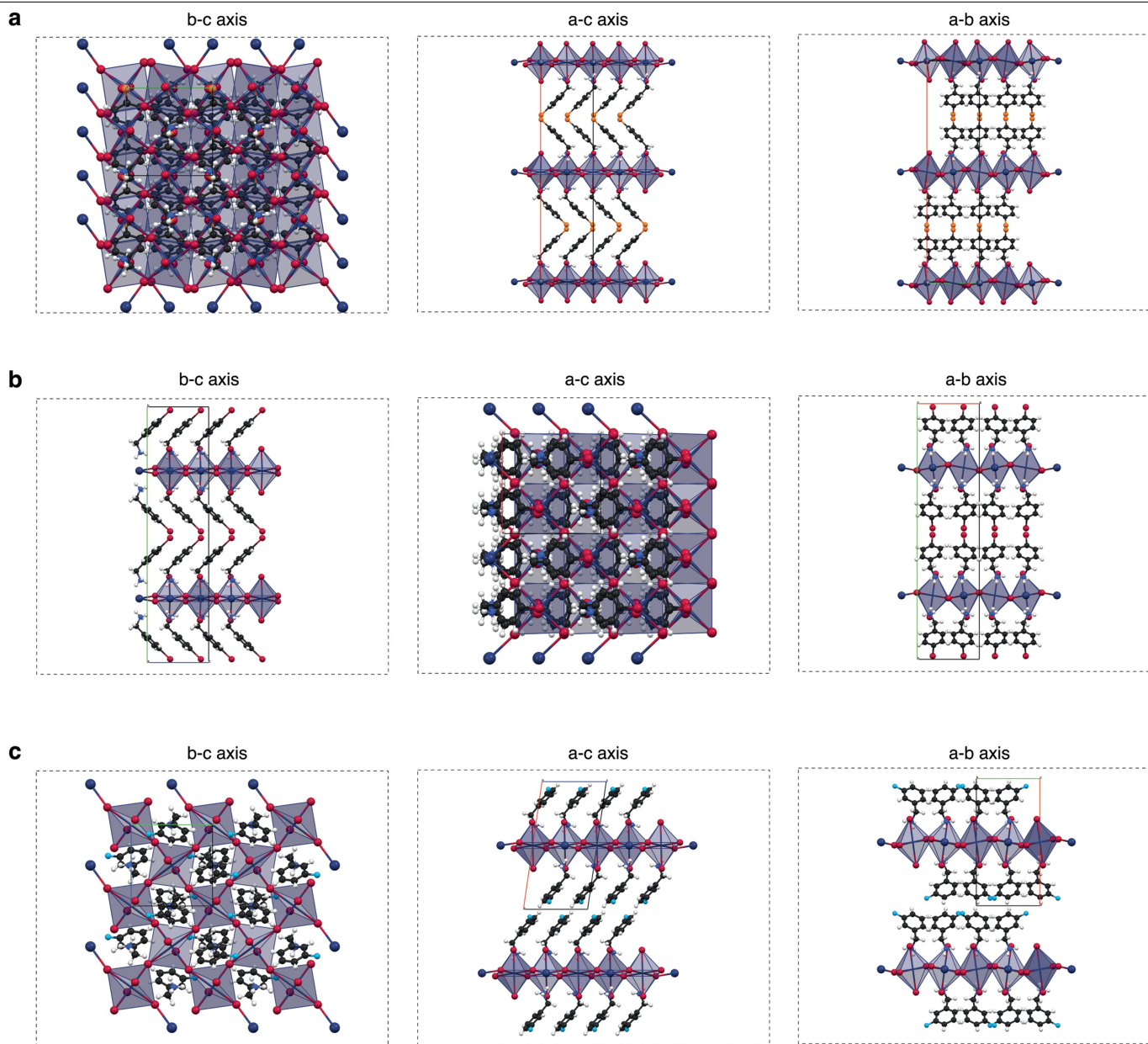
Extended Data Fig. 3 | Crystal structure of a. (4Br-PMA)$_2$GeI$_4$; **b**, (4I-PMA)$_2$GeI$_4$; **c**, (3F-PMA)$_2$GeI$_4$ with indicated view axis.
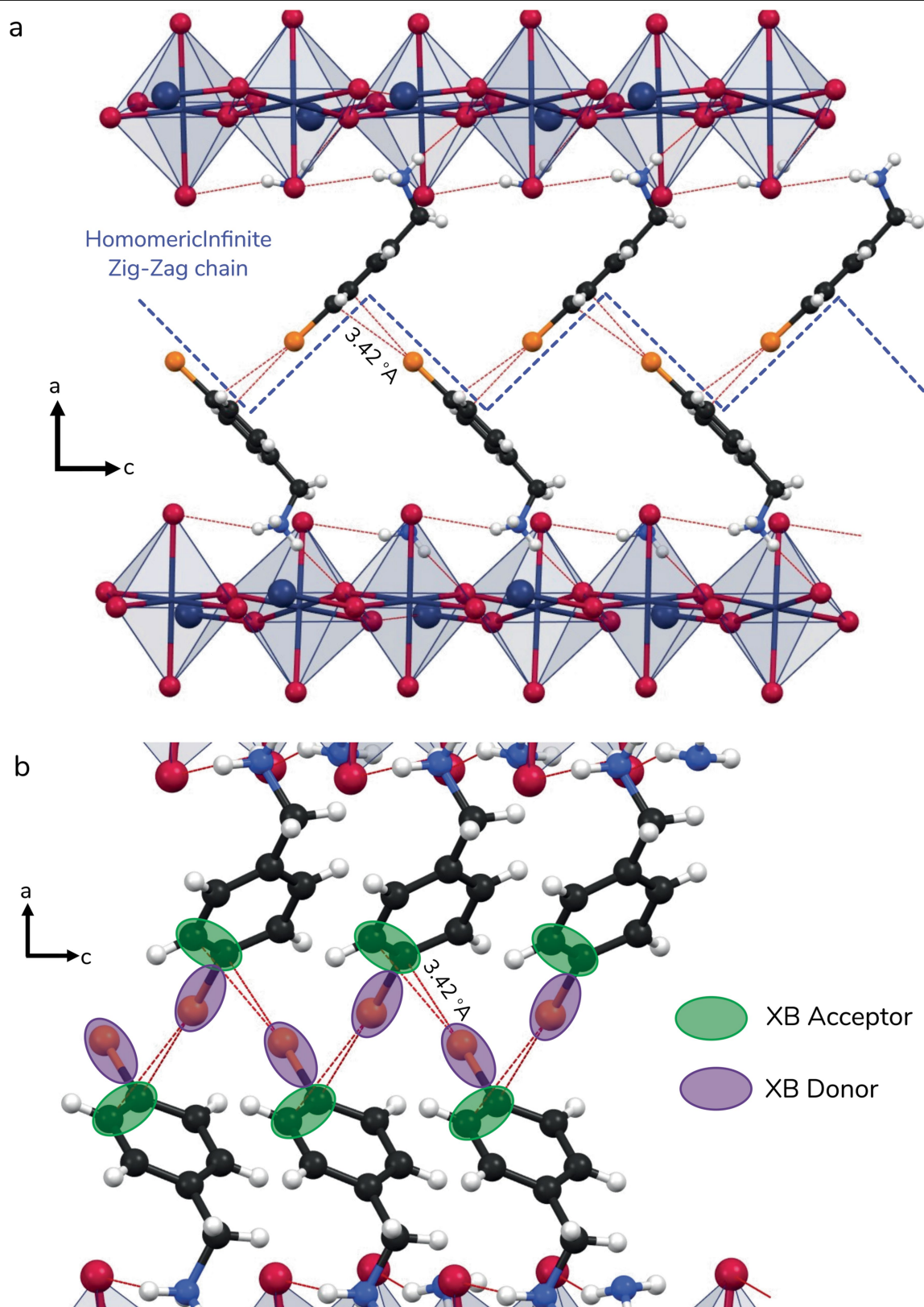
Extended Data Fig. 4 | Halogen bonding network in the Germanium perovskite structure using Br-PMA as the cation. a, view at the a-c crystal axis of the crystal. **b**, Titled view to show donor and acceptor sites of the XB bonding.
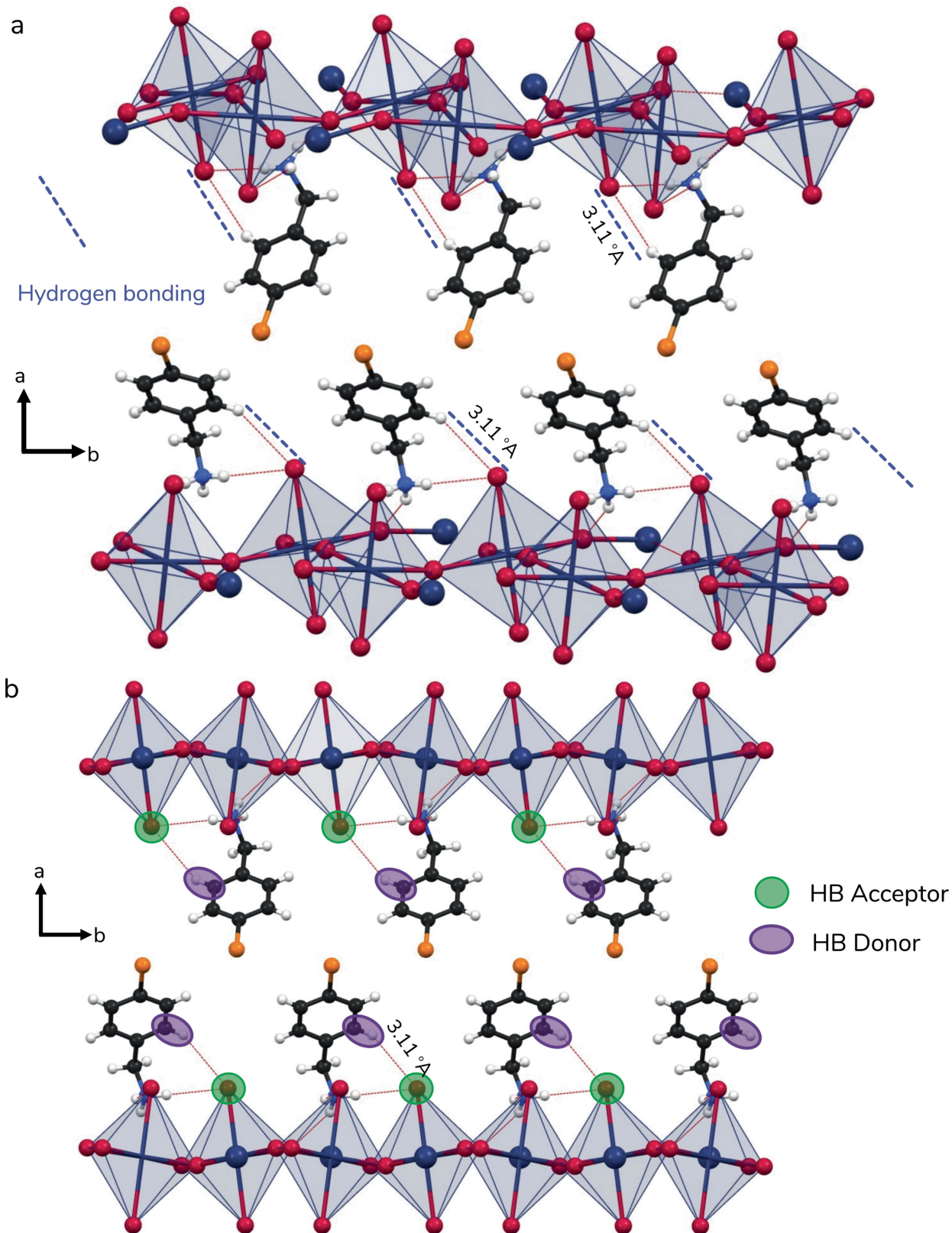
Extended Data Fig. 5 | Hydrogen bonding between the organic module and inorganic framework using F-PMA as the cation. a, View at the a-b crystal axis. **b**, titled view to show donor and acceptor sites of the HB bonding.
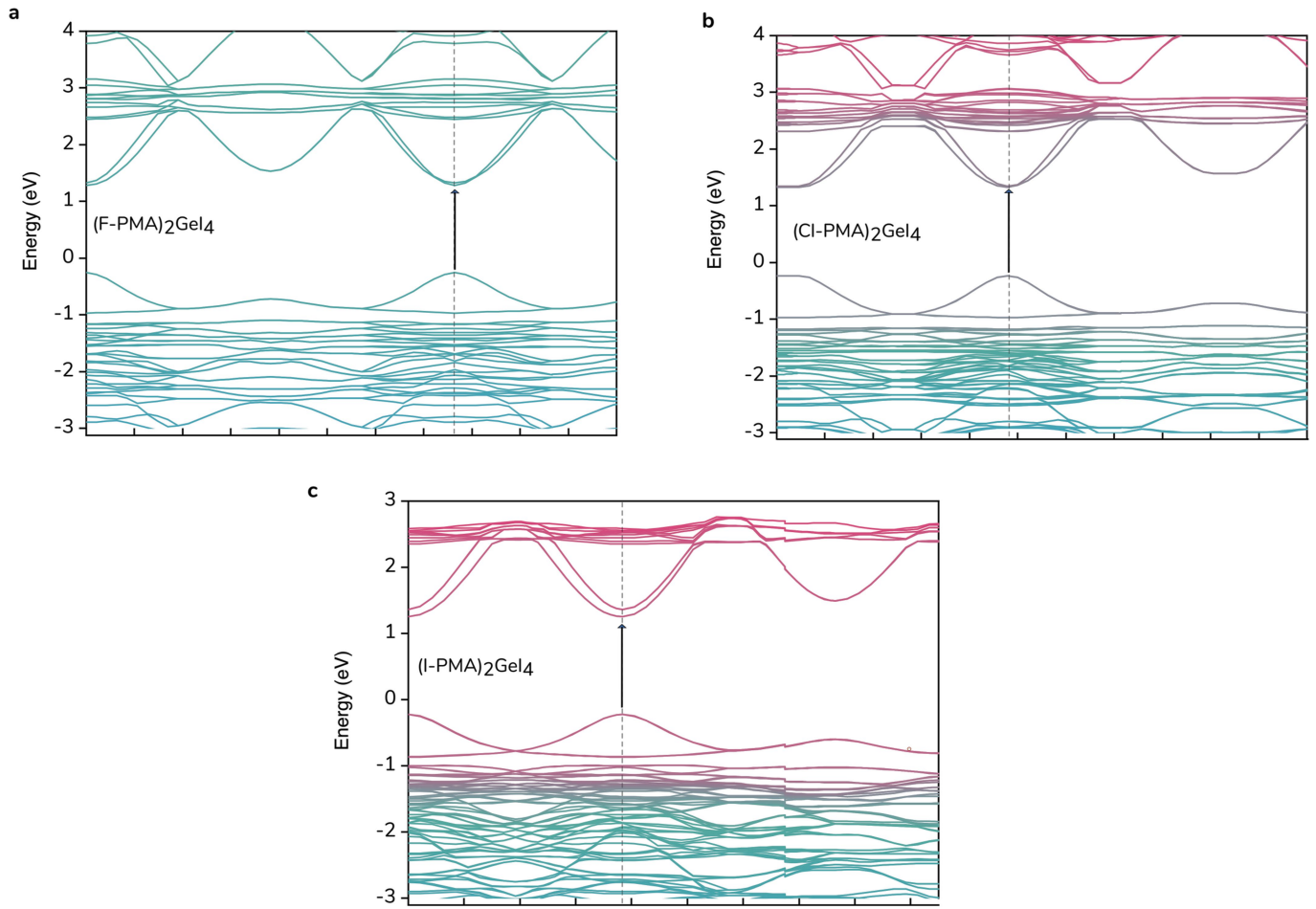
Extended Data Fig. 6 | DFT Calculated electronic band structure (total contribution) of the Ge perovskite. using: **a**, F-PMA; **b**, Cl-PMA; **c**, I-PMA as cations.

a Conduction band   Valence band

b Conduction band   Valence band

c Conduction band   Valence band
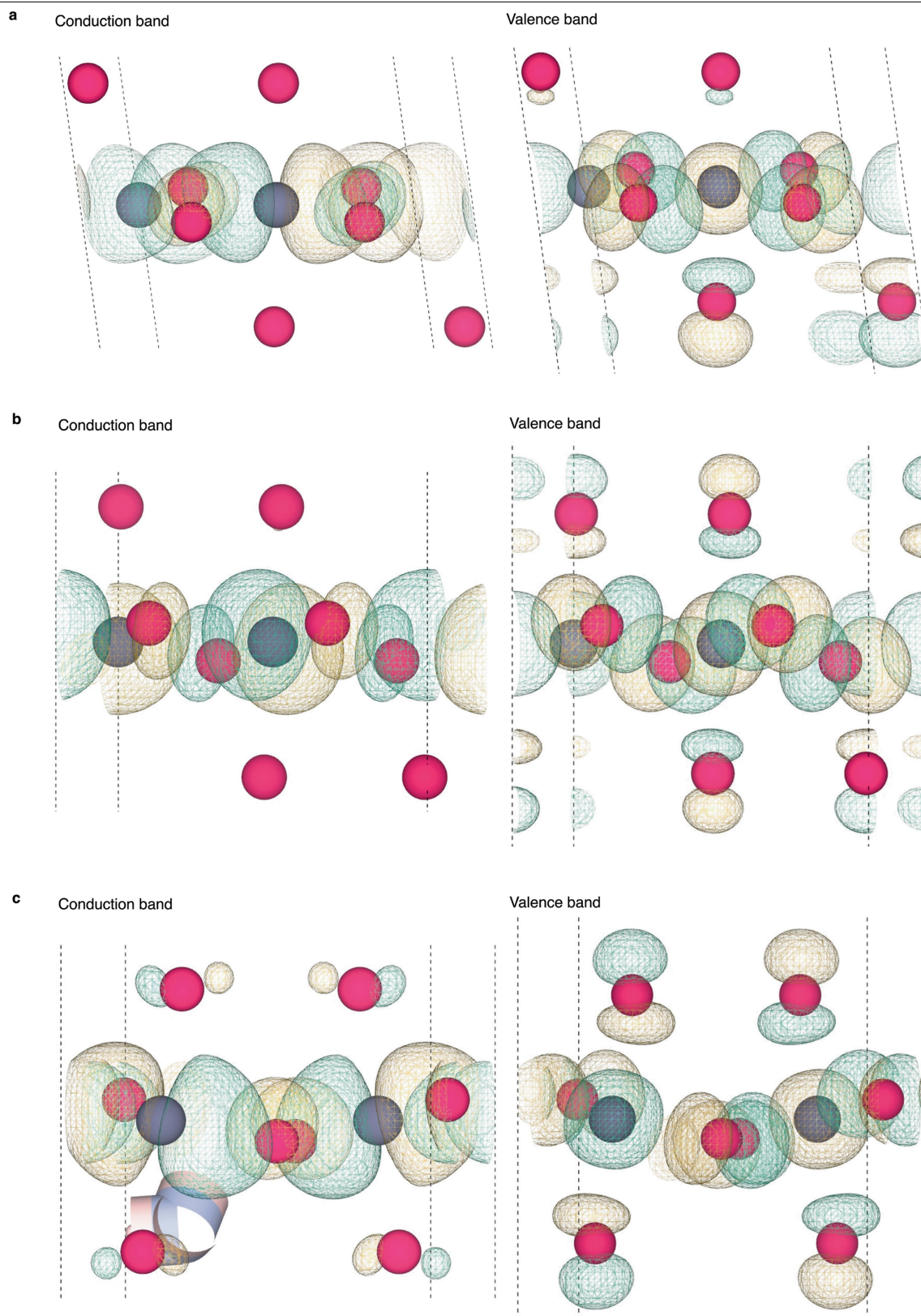
Extended Data Fig. 7 | Charge density mapping of conduction (CB) and valence band (VB) in the Ge perovskite. using: **a**, F-PMA; **b**, Cl-PMA; **c**, I-PMA as cations. Note that for both cases, the contribution of the density of state on the organic parts is negligible, and thus organic molecules are not shown in the figure. Dark grey and red sphere represent the Ge and I atoms, respectively. Green and yellow colours are used for representation of positive and negative isosurfaces.

a
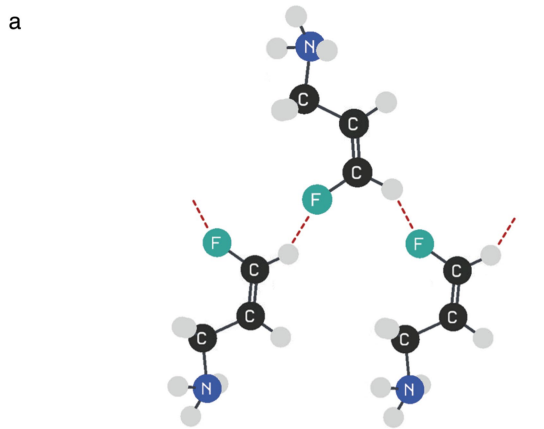
- Aliphatic backbone
- Hydrogen bonding between F and H
- Double bond keeps the structure rigid

b
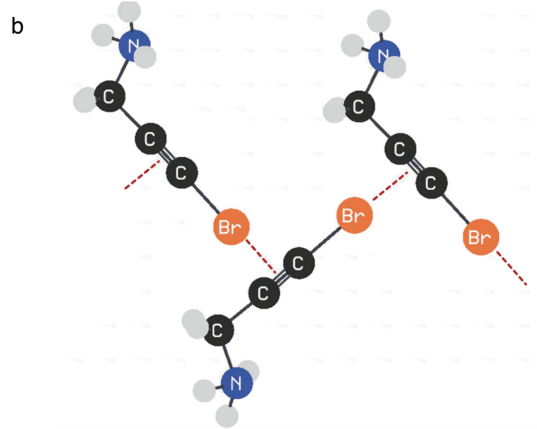
- Aliphatic backbone
- Halogen bond between Br and pi electrons
- Triple bond keeps the structure rigid
and hold Br at the elongation of c-c bond

c
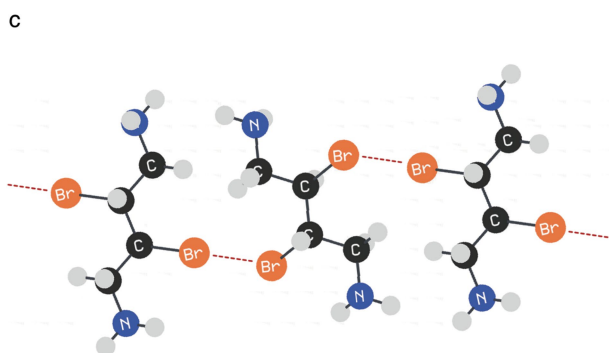
- Aliphatic backbone in DJ structure
- Halogen bond between Br atoms
- Depends on emerged 3D geometry, Br atoms
  may interact by Type-I or Type-II halogen bonding

d
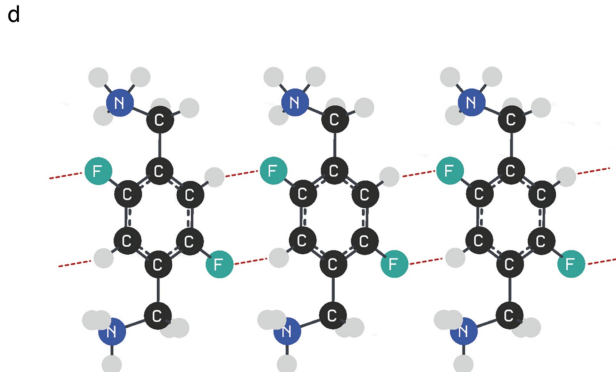
- Aromatic backbone in DJ structure
- Possiblity of four hydrogen bonds for each molecules
- Hydrogen bonds may extent in different directions

e
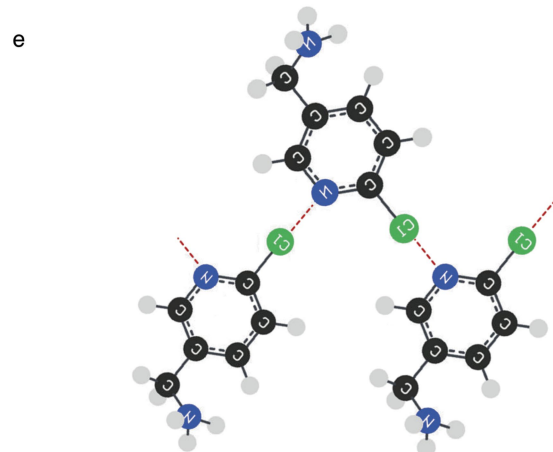
- Aromatic backbone
- Halogen bond between the Cl and N lone pair
- Nitrogen could be in the ortho possition

Extended Data Fig. 8 | Organic design examples that potentially satisfy the criteria for extension of homomeric bonds. Each example includes the possible route for the propagation of intermolecular bonding.

Extended Data Table 1 | Distortion index of the previously published germanium perovskites

CRYSTAL CODE	P-1	P-2	P-3	P-4	P-5	P-6	P-7	P-8
ANION SITE	Cl	Cl	Br	Br	Br	Br	I	I
CATION SITE	Pyridine	CD3ND3	4Br-PEA	PMA	4F-PEA	PEA	But-A	PEA
SPACE GROUP	$P\,2_1/c$	$Pna2_1$	$Pna2_1$	P 1	$P\,2_1/c$	P 1	$Pcmn$	P 1
GE-I BOND LENGTH (Å)	2.325	2.305	2.658	2.527	3.314	2.548	2.838	2.81
	3.433	2.3058	2.596	3.288	2.559	3.337	3.217	3.307
	3.385	2.3058	2.559	2.56	2.553	2.556	3.059	2.778
	2.322	3.3595	3.226	3.131	3.282	3.247	3.016	3.362
	2.301	3.3595	2.559	2.611	3.301	3.297	2.838	3.374
	4.558	3.3595	3.26	3.282	2.583	2.548	3.217	2.821
GE-I AVERAGE BL (Å)	3.054	2.833	2.810	2.900	2.932	2.922	3.031	3.075
BAUR DISTORTION INDEX, %	24.17	18.60	10.28	11.51	12.52	12.71	4.40	8.86
REFERENCE	44	45	46	46	46	46	47	48

CRYSTAL CODE	P-9	P-10	P-11	P-12	P-13	P-14	P-15
ANION SITE	I	I	I	I	I	I	I
CATION SITE	Cs	CH_3NH_3	$HC(NH_2)_2$	$CH_3C(NH_2)_2$	$C(NH_2)_3$	$(CH_3)_3NH$	$(CH_3)_2C(H)NH_3$
SPACE GROUP	R3m	R3m	R3m	$P\,2_1$	$P\,2_1/c$	$P6_3$	$I\,4\,2\,d$
GE-I BOND LENGTH (Å)	2.753	2.772	2.773	2.745	2.907	2.872	2.708
	3.256	3.446	3.577	3.598	3.259	3.332	2.708
	2.753	2.772	2.773	2.738	3.417	3.019	3.634
	3.256	3.446	3.577	3.646	2.778	3.1	3.634
	2.753	2.772	2.773	3.559	3.389	2.991	2.604
	3.256	3.446	3.577	2.764	2.784	3.13	2.65
GE-I AVERAGE BL (Å)	3.005	3.109	3.175	3.175	3.089	3.074	2.990
BAUR DISTORTION INDEX, %	8.37	10.84	12.66	13.42	8.61	3.69	14.37
REFERENCE	2	2	2	2	2	2	2

Article

Extended Data Table 2 | Crystallographic characteristics of the synthesized germanium perovskites

COMPOUND NUMBER [A]	1	2	3	4	5	6	7	8	9
CATION	PMA	4F-PMA	4Cl-PMA	4Br-PMA	4I-PMA	CF3-PMA	3F-PMA	3Cl-PMA	4F-PEA
CRYSTAL SYSTEM	Monoclinic	Monoclinic	Orthorhombic	Orthorhombic	Orthorhombic	Orthorhombic	Monoclinic	Monoclinic	Triclinic
SPACE GROUP	P21	P21/c	Pccn	Pccn	Ccc2	Pna21	P21/c	P21/c	P-1
GE-I BOND LENGTH (Å)	2.869	2.9796	2.968	2.9705	2.972	2.954	2.9736	2.9855	3.41
	2.8464	2.9796	2.968	2.9705	2.971	3.256	2.9736	2.9855	2.803
	2.8766	2.9789	2.9686	2.9728	2.971	3.227	2.9772	2.9879	2.807
	3.202	2.9789	2.9963	2.9728	2.972	2.806	2.9772	2.9879	3.313
	3.238	2.9969	2.9963	2.9903	2.994	3.023	2.9985	3.0088	2.779
	3.192	2.9969	2.9686	2.9904	2.994	2.82	2.9985	3.0088	3.343
GE-I AVERAGE BL (Å)	3.037	2.985	2.978	2.978	2.979	3.014	2.983	2.994	3.076
GE-I-GE ANGLE (°) [B]	-	157	156	157	165	-	155.7	155	-
INTERLAYER DISTANCE (Å)	6.68	5.42	5.18	5.12	5.1	5	5.38	5.18	6.18
BAUR DISTORTION INDEX, %	5.71	0.26	0.42	0.28	0.34	5.12	0.34	0.33	9.13
INTERMOLECULAR BONDING	C-H --- C	C-H --- I-Ge	C-H --- I-Ge	C-H --- I-Ge	C-H --- I-Ge	C-N---I-Ge	C-H --- I-Ge	C-H --- I-Ge	C-H --- I-Ge
	non-specific	C-F --- H-C	C-Cl --- CC	C-Br --- CC	C-I --- CC	-	C-F --- H-C	C-Cl --- H-C	C-F --- H-C
HOMOMERIC BONDING	NO	Yes	Yes	Yes	Yes	NO	Yes	Yes	Yes
PEROVSKITE POLYHEDRAL TYPE	Mix of GeI$_3$ and GeI$_4$	GeI$_6$	GeI$_6$	GeI$_6$	GeI$_6$	GeI$_4$	GeI$_6$	GeI$_6$	GeI$_3$

COMPOUND NUMBER	10	11	12	13	14	15	16	17	18
CATION	4Cl-PEA	4OH-PEA	A-Pyr	But-A	DiA-Pyr	I-EA	OH-EA	Morph	MaGeI3
CRYSTAL SYSTEM	Orthorhombic	Triclinic	orthorhombic	orthorhombic	Triclinic	Monoclinic	Orthorhombic	Monoclinic	Trigonal
SPACE GROUP	Pna21	P-1	Pca21	P212121	P-1	P21/n	Pnma	P21/m	R3m
GE-I BOND LENGTH (Å)	2.798	2.801	2.74	3.047	2.7618	2.767	2.709	2.704	2.772
	3.421	2.792	3.461	3.07	2.8404	2.782	2.746	2.779	2.772
	2.792	2.775	3.086	2.815	2.9605	2.909	3.056	3.036	2.772
	2.815	3.265	3.059	3.219	3.0532	3.356	3.368	3.785	3.446
	3.367	3.334	3.053	2.806	3.1802	3.359	3.937	3.523	3.446
	2.912	3.44	3.13	3.237	3.5341	3.11	3.056	3.036	3.446
GE-I AVERAGE BL (Å)	3.018	3.068	3.088	3.032	3.055	3.047	3.145	3.144	3.109
GE-I-GE ANGLE (°)	-	-	-	-	-	-	-	-	-
INTERLAYER DISTANCE (Å)	7.18	5.34	8.6	6.4	6.23	7.04	9.14	7.66	14.5
BAUR DISTORTION INDEX, %	8.32	9.06	4.48	4.88	4.54	7.48	10.75	10.82	10.84
INTERMOLECULAR BONDING	C-H --- I-Ge	H-O --- H-C	C-H --- I-Ge	-	N-H---I-Ge	C-I---C-I	H-O----H-N	C-O --- H-C	-
	C-Cl --- C-C	C-H --- I-Ge	-	-	-	N-H---I-Ge	H-O----I-Ge	-	-
HOMOMERIC BONDING	Yes	NO	NO	NO	NO	NO	NO	NO	-
PEROVSKITE POLYHEDRAL TYPE	GeI$_4$	GeI$_3$	GeI$_3$	GeI$_4$	GeI$_4$	GeI$_3$	GeI$_4$	GeI$_4$	GeI$_4$